

# Tensor-network methodology for super-moiré excitons beyond one billion sites

Anouar Moustaj <sup>1,\*</sup> Yitao Sun <sup>1,\*</sup> Tiago V. C. Antão <sup>1</sup> Lumen Eek <sup>2</sup> and Jose L. Lado <sup>1</sup>

<sup>1</sup>*Department of Applied Physics, Aalto University, 02150 Espoo, Finland*

<sup>2</sup>*Institute of Theoretical Physics, Utrecht University, Utrecht, 3584 CC, Netherlands*

(Dated: March 11, 2026)

Computing excitonic spectra in quasicrystal and super-moiré systems constitutes a formidable challenge due to the exceptional size of the excitonic Hilbert space. Here, we demonstrate a tensor-network method for the real-space Bethe-Salpeter Hamiltonian, allowing us to access the spectra of an excitonic  $10^{18}$ -dimensional Hamiltonian, and enabling the direct computation of bound-exciton spectral functions for systems exceeding one billion lattice sites, several orders of magnitude beyond the capabilities of conventional approaches. Our method combines a tensor-network encoding of the real-space Bethe-Salpeter Hamiltonian with a Chebyshev tensor network algorithm. This strategy bypasses explicit storage of the Hamiltonian while preserving full real-space resolution across widely different length scales. We demonstrate our methodology for one- and two-dimensional super-moiré systems, achieving the simultaneous resolution of atomistic and mesoscopic structures in the excitonic spectra in billion-size systems, showing exciton miniband formation and moiré-induced spatial confinement. Our results establish a real-space methodology enabling the simulation of excitonic physics in large-scale quasicrystal and super-moiré quantum matter.

*Introduction* Two-dimensional (2D) van der Waals materials provide an excellent platform for engineering excitonic matter owing to their enhanced Coulomb interactions. This has led to pronounced excitonic features that remain stable even at room temperature [1–3], making these platforms ideal for technological applications [4–9]. Importantly, control over twist angle and lattice mismatch in multilayer transition metal dichalcogenides (TMD) has enabled the realization of moiré excitons [10–16] by producing an effective potential landscape that modulates the coupling of electron and hole pairs across both layers, leading to emergent phenomena, such as periodic confinement and excitonic minibands. These excitons can also become strongly localized at moiré trapping sites, forming programmable arrays of quantum emitters or allowing the engineering of exciton lattices that function as artificial quantum simulators [10, 16, 17].

Microscopically, excitonic phenomena can be predicted from the Bethe-Salpeter equation (BSE), which incorporates the single-particle electronic structure and the screened electron-hole interaction [18–24]. While for periodic systems a momentum space formulation of excitons is successful, for incommensurate modulations, such as those arising in moiré materials, a fully real-space formulation for excitonic effects becomes inevitably necessary. In these cases, conventional methods face severe computational limitations, as even at the single-particle level, real-space methods scale poorly with system size [19, 23–27]. For excitons, the situation is more demanding, since the two-particle Hilbert space scales quadratically with the number of lattice sites. In super-moiré materials, where characteristic length scales can exceed those of standard moiré systems by orders of magnitude, the effective lattice may involve millions or even billions of sites [28, 29], rendering brute-force approaches computationally prohibitive.

In the single-particle case, quantum many-body solvers based on tensor networks (TNs) have enabled the treatment of exponentially large Hamiltonians [30–33]. These approaches avoid explicit storage of large matrices by representing operators and states with TNs: many-body factorizations that permit algebraic manipulations in exponentially large Hilbert spaces [34–45]. The required tensor representations are constructed using tensor cross interpolation techniques [46–52]. Similarly, the employment of TNs to encode classical functions has led to speedups of several orders of magnitude across diverse computational settings [49, 53–59], including applications in computational chemistry [60] and dynamical simulations [61–66]. These developments have enabled, among others, the study of quasicrystalline mosaics of topological Chern states [32], the self-consistent solution of interacting super-moiré systems at scales exceeding one billion lattice sites [31], and the direct computation of spatially-dependent momentum-resolved spectral function of large nonperiodic systems [33].

Here, we demonstrate a tensor-network (TN) based methodology to access the real-space exciton spectra in super-moire systems. Our methodology relies on combining a real-space TN representation of the electron-hole Hilbert space, and tensor-network kernel polynomial Chebyshev algorithms with a high-resolution spectral kernel. Our approach enables the solution of the real-space BSE on lattices exceeding one billion sites, both in 1D and 2D, surpassing by many orders of magnitude the capabilities of conventional BSE solvers [23, 24]. We show that these techniques allow probing the emergence of exciton moire minibands, together with imaging the microscopic exciton localization, both in quasicrystalline and super-moire systems.

*Tensor Network Methodology* For concreteness, we formulate our algorithm in a minimal two-band model

that captures excitonic physics, and we solve it with our TN methodology. We take an interacting Wannier Hamiltonian for the valence and conduction band of a semiconductor as  $\hat{H} = \hat{H}_c + \hat{H}_v + \hat{H}_U$ , with

$$\begin{aligned} \hat{H}_b &= \sum_{l,m} t_{lm} c_{b,l}^\dagger c_{b,m} + \sum_l V_{b,l} c_{b,l}^\dagger c_{b,l}, \\ \hat{H}_U &= \sum_l U_l c_{c,l}^\dagger c_{c,l} c_{v,l}^\dagger c_{v,l}, \end{aligned} \quad (1)$$

where  $c_{c,l}^\dagger$  ( $c_{v,l}^\dagger$ ) creates an electron in the Wannier conduction (valence) band at site  $l$ . The band index is denoted by  $b = c, v$  for conduction and valence, respectively. The hopping amplitudes are given by  $t_{lm}$ , while  $V_{c,l} = -V_{v,l}$  represents the on-site potential, and  $U_l$  describes the local screened electrostatic interaction between a conduction-band Wannier state and a valence-band Wannier state. This Hamiltonian stems from projecting a microscopic interacting electron model onto the low-energy subspace spanned by the top valence and bottom conduction bands, performing a Wannier transformation to real space, and retaining the local Coulomb interaction between valence and conduction bands. Our objective is to solve the effective two-particle Hamiltonian obtained from the BSE by projecting the many-body Hamiltonian Eq. (1) onto the variational exciton state  $|l, m\rangle = c_{c,l}^\dagger c_{v,m} |\Omega\rangle$ , where  $|\Omega\rangle = \prod_{l=1}^N c_{vl}^\dagger |0\rangle$  is the Fermi sea, filled with  $N$  electrons. The specific matrix takes the form

$$\hat{H}_X = \hat{T}_c \otimes \mathbb{1} - \mathbb{1} \otimes \hat{T}_v - \hat{U}, \quad (2)$$

where  $\hat{T}_c$  contains both the conduction hopping term and an additional contribution from the local Coulomb interaction,  $\hat{T}_v$  is the contribution arising from the valence band, and  $\hat{U}$  couples electrons and holes on the same site. Its matrix elements are  $U_{klmn} = U_k \delta_{kl} \delta_{mn} \delta_{ln}$  and, as such, cannot be written as a product operator (see SM [67] for details).

The key strategy of our methodology lies in the encoding of  $2^L$  real-space sites of the Wannier tight-binding Hamiltonian into  $L$  pseudo-spin indices [30–33] for each sector of the BSE Hamiltonian, effectively resulting in a system of  $2L$  pseudo-spin degrees of freedom. In this pseudo-spin basis, the single-particle Hamiltonian of each sector can be written as a TN matrix product operator (MPO) of the form  $\mathcal{H}_{(s_1, s_2, \dots, s_L), (s'_1, s'_2, \dots, s'_L)} = \Gamma_1^{s_1, s'_1} \Gamma_2^{s_2, s'_2} \dots \Gamma_L^{s_L, s'_L}$ . Each tensor  $\Gamma_r$  carries four indices: two virtual indices, which are contracted with neighboring tensors, and two physical indices associated with the local 2D Hilbert space  $s_r, s'_r$ . The virtual indices have dimension  $\chi_r$ , referred to as the bond dimension, which determines the expressiveness of the local tensor. The explicit form of the tensors can be obtained with quantum tensor cross interpolation [48, 49, 53–58], enabling the representation of spatially varying Hamiltonians as a TN. Considering the first two terms of

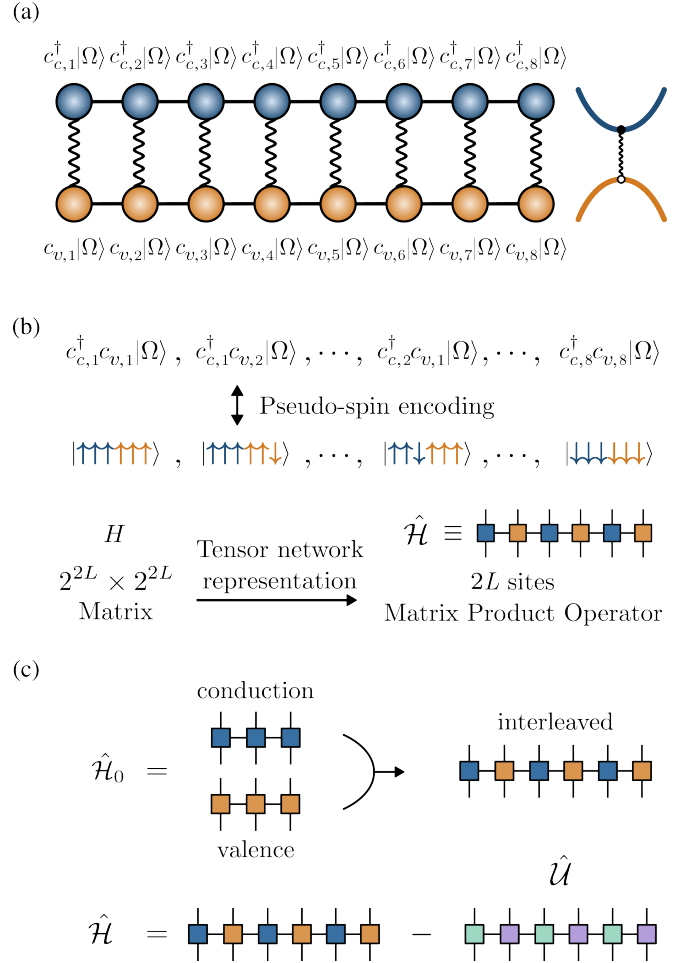


FIG. 1. (a) Schematic of the exciton Hamiltonian, with purple corresponding to the conduction band and light brown to the valence band, together with their corresponding single-particle basis. (b) The encoding of the two-particle  $2^{2L} \times 2^{2L}$  Hamiltonian matrix into a  $2L$  pseudo-spin MPO. (c) The combination of the single-particle Hamiltonians and the interaction kernel using interleaved ordering.

Eq. (2), a straightforward many-body encoding consists of two independent pseudo-spin chains of length  $L$ , which together form a composite chain of length  $2L$ , reflecting the direct-product structure of the corresponding operators. However, in this pseudo-spin representation, the interaction operator is expressed as  $\hat{U} = \prod_{r=1}^L (\frac{1}{2} \mathbb{1}_r \otimes \mathbb{1}_{r+L} + 2\sigma_r^z \sigma_{r+L}^z)$ . This specific form couples the two pseudo-spin chains by sequentially ordering all electron sites before all hole sites. Such a layout leads to an exponential growth of the bond dimension at the interface between the two MPOs as the system size increases. To mitigate this, we use a more efficient interleaved ordering [50, 53] of the sites, which maintains a constant bond dimension for the interaction operator regardless of the system size. In essence, rather than linking the individual pseudospin blocks with a single internal bond at their interface, we adopt an interleaved

ordering in which the tensor cores are rearranged so that each local electron pseudospin degree of freedom is directly coupled to its corresponding hole pseudospin degree of freedom. The MPO construction of the Hamiltonian is illustrated in Fig. 1 [68].

The excitonic spectral signatures can be obtained with a Chebyshev TN kernel polynomial algorithm (KPM) [69]. This allows for a direct calculation of the strictly localized bound exciton local density of states (LDOS),  $\rho(\mathbf{r}, E) = \langle \mathbf{r}, \mathbf{r} | \delta(E - \hat{H}) | \mathbf{r}, \mathbf{r} \rangle$ . The exciton LDOS is expanded as

$$\rho(\mathbf{r}, \tilde{E}) = \frac{1}{\pi\sqrt{1 - \tilde{E}^2}} \left[ 1 + 2 \sum_{n=1}^{\infty} \mu_n(\mathbf{r}) T_n(\tilde{E}) \right],$$

where  $T_n(\tilde{E})$  are Chebyshev polynomials of a rescaled energy  $\tilde{E} \in (-1, 1)$  and  $\mu_n(\mathbf{r})$  are the Chebyshev moments. These constitute the core building blocks of the present methodology and are constructed according to the recursion relations [69]

$$\begin{aligned} \mu_n(\mathbf{r}) &= \langle \mathbf{r}, \mathbf{r} | \nu_n \rangle, \\ |\nu_n\rangle &= 2\hat{H}|\nu_{n-1}\rangle - |\nu_{n-2}\rangle, \\ |\nu_0\rangle &= |\mathbf{r}, \mathbf{r}\rangle, \quad |\nu_1\rangle = \hat{H}|\nu_0\rangle. \end{aligned} \quad (3)$$

In practice, the expansion is truncated to  $N_\mu$  terms. Within the KPM framework, the inclusion of the Jackson kernel [70] yields an effective energy resolution of order  $1/N_\mu$ , thereby setting the scale of the associated spectral broadening [69]. For 2D systems, however, the rapid growth of the bond dimension with the number of Chebyshev moments necessitates an alternative strategy. To keep  $N_\mu$  moderate while maintaining spectral resolution, we employ a high-order delta-Chebyshev (HODC) kernel [71], which enables independent control of the KPM truncation error through additional parameters  $\eta$  and  $m$ , achieving a faster convergence of order  $\eta^m \sim 1/N_\mu^m$  (see SM [67] for details).

We now demonstrate the capabilities of our TN framework by applying it to two representative examples that require the simultaneous resolution of both macroscopic and atomistic length scales.

*1D incommensurate super-moiré potential* The first example is a 1D system subject to a modulated single-particle on-site potential of the form

$$V_i = V_0 \left[ 1 + 0.1 \cos\left(\frac{\pi x_i}{3\sqrt{5}}\right) + 0.1 \cos\left(\frac{5\pi x_i}{N\sqrt{3}}\right) \right], \quad (4)$$

where the two modulations are incommensurate with each other. This model captures moiré physics in quasi-one-dimensional van der Waals materials [72–74] or multi-walled nanotubes [75–79]. The first cosine induces a small-scale modulation, while the second induces a large-scale one. We also consider nearest-neighbor uniform hopping  $t$ , a constant electron-hole interaction

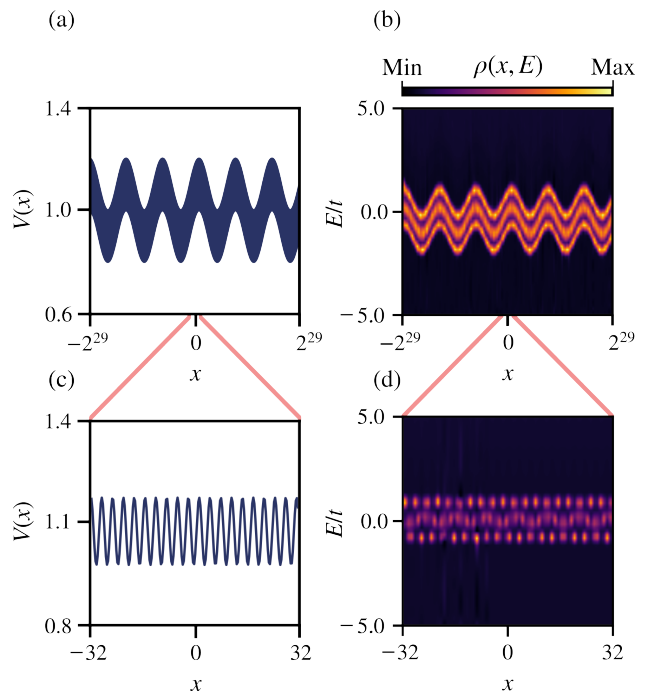


FIG. 2. (a) Spectral band in real space of the bound super-moiré excitons, together with a zoom of the central region of linear extent  $\ell = 64$ . (b) Super-moiré on-site potential modulation, with a corresponding zoom of the central region of length  $\ell = 64$ . The outlined region is not shown to scale with respect to the full domain and serves only as a visual guide.

strength  $U = 5t$ , and an on-site potential strength  $V_0 = 3t$ . Figure 2(a) shows the large-scale modulation Eq. (4) for a system of  $N = 2^{30}$  sites and Fig. 2(b) the corresponding large-scale LDOS as a function of energy. The isolated exciton band in real-space closely follows the spatial profile of the on-site modulation potential. In Fig. 2(c) and Fig. 2(d) provide a zoom into the central region of length  $\ell = 64$  of the same quantities as in Fig. 2(a,b). The spatial modulation and its imprint in the LDOS are also well resolved at the atomic scale. Furthermore, the incommensurability of the small-scale modulation frequency gives rise to miniband splitting, which is visible at both length scales through the modulated small gap.

*2D quasiperiodic incommensurate super-moiré potential* We now demonstrate the methodology on a 2D super-moiré quasicrystal. We consider a square lattice with an on-site potential exhibiting an eight-fold quasiperiodic, incommensurate modulation at both small and large scales.

$$V(\mathbf{r}) = V_0 \left[ 1 + \sum_{n=1}^4 (\Delta_\alpha \cos(\alpha \mathbf{k}_n \cdot \mathbf{r}) + \Delta_\beta \cos(\beta \mathbf{k}_n \cdot \mathbf{r})) \right], \quad (5)$$

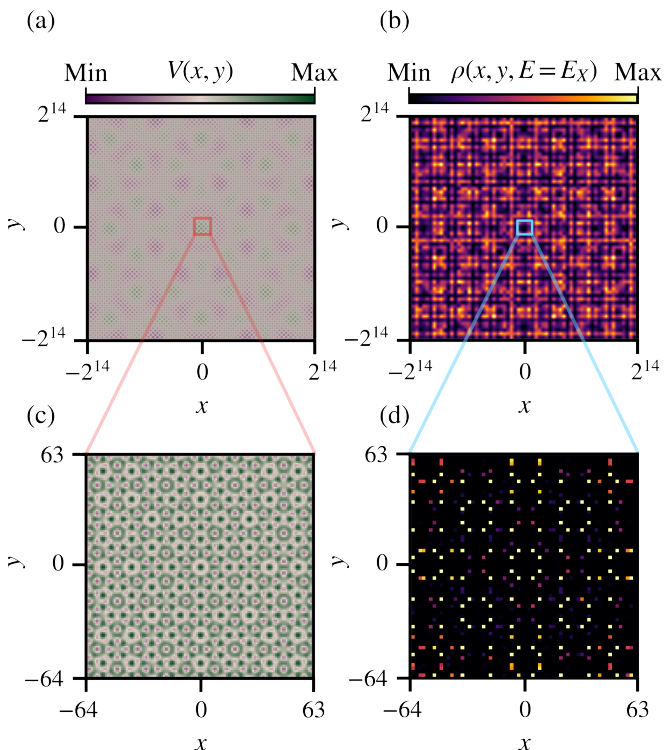


FIG. 3. (a) 2D exciton LDOS  $\rho(x, y, E = E_X)$  evaluated at the bound-exciton energy  $E = E_X$ , together with a zoom of the central region of area  $A = 128 \times 128$ . (b) Corresponding on-site potential, with an analogous zoom of the central region of area  $A = 128 \times 128$ . The square outline is not drawn to scale relative to the full domain and is included as a visual guide.

where  $\Delta_\alpha$  sets the modulation amplitude at the atomic scale, while  $\Delta_\beta$  determines the super-moiré modulation amplitude. The eightfold pattern is created by the superposition of four wave vectors given by  $\mathbf{k}_n = R^n(\pi/4) [2\pi, 0]^T$ , with  $R(\pi/4)$  denoting the 2D rotation matrix corresponding to an angle of  $\pi/4$  radians. This potential can result from the superposition of two square lattice monolayers rotated at  $45^\circ$  relative to each other, as in twisted GeX/SnX moiré superlattices [80]. We set  $\Delta_\alpha = 0.15$ ,  $\Delta_\beta = 0.05$ , and take moiré length scales  $\alpha = 2/(5\sqrt{5})$  and  $\beta = 16/(\sqrt{3}N_x)$ . The uniform nearest-neighbor hopping is  $t$ , the on-site modulation potential amplitude  $V_0 = 6t$ , and the local Coulomb interaction  $U = 12t$ . The large-scale modulation landscape of the on-site potential is shown in Fig. 3(a) for a system of size  $N_x = N_y = 2^{15}$ , corresponding to more than a billion lattice sites. In Fig. 3(b), the corresponding LDOS at the bound exciton energy  $E_X = -4t$  is depicted, where one can observe that the spectral weight peaks near the minima of the on-site potential, indicating spatial confinement of the excitons in a pattern with eight-fold rotational symmetry. In Fig. 3(c) and Fig. 3(d), a zoom into a central region of area  $A = 128 \times 128$  is shown for the on-site potential and LDOS respectively. Similarly to the

super-moiré length scale, the same eightfold-symmetric confinement pattern at the minima of the potential can be observed at the atomic length scale.

*Discussion* The present results establish a scalable real-space framework for solving the BSE in regimes that are inaccessible to conventional approaches. In contrast to standard implementations, whose cost scales quadratically with the number of lattice sites and which require explicit storage of the two-particle Hamiltonian, our formulation exploits the TN structure to achieve logarithmic scaling with system size and efficient TN compression. This enables the treatment of super-moiré systems with effective Hamiltonian dimensions of order  $10^{18}$ , a regime far beyond existing methodologies. It is worth noting that several limitations remain. In 2D, the rapid growth of bond dimensions with the number of Chebyshev moments places us near the threshold of efficient compressibility, currently limiting our accuracy to approximately forty moments. While the HODC kernel partially mitigates this by resolving spatial features of the LDOS at lower expansion orders, alternative architectures such as tree TNs [81] may be better suited to handle 2D correlations and further enhance performance. While we have focused here on local electron-hole interactions in minimal 1D and 2D lattices for concreteness, the framework can be systematically extended to incorporate long-range Coulomb interactions and exchange terms within the same TN formalism, as well as to more complicated lattice geometries. Such extensions would facilitate the quantitative modeling of realistic moiré heterostructures while preserving their real-space scalability demonstrated here. It is finally worth noting that the inclusion of long-range interactions and exchange terms may potentially accelerate the growth of the bond dimension, further motivating the development of alternative TN architectures. Beyond the specific exciton problem we have focused on here, our methodology provides a general strategy for addressing two-body correlation problems directly on real-space lattices [82]. This technique can be applicable to other correlated states, including the formation of bipolaron states in moiré systems [83–85] and bimagnon bound states in moiré magnetic insulators [86–91]. In all such cases, under appropriate circumstances, computations involve a two-particle Hilbert space whose direct treatment becomes prohibitive at large system sizes, yet can be efficiently encoded within the present TN framework.

*Conclusion* We have demonstrated a TN methodology that enables direct real-space calculations of bound-exciton spectral functions in exponentially large lattices. Our approach combines a pseudo-spin TN encoding of the BSE Hamiltonian, including both the single particle and many-body interaction in the full two-particle excitonic space. Our algorithm leverages an interleaved representation of the electron-hole BSE space, together with a TN-based kernel polynomial expansion enhanced

by a higher-order delta Chebyshev spectral kernel. We demonstrated our methodology for 1D and 2D incommensurate super-moiré potentials with more than a billion sites, demonstrating the simultaneous resolution of atomistic and mesoscopic structures in the exciton LDOS. In both cases, we show the bound exciton spectral signatures in real space following the spatial modulation landscape. In 1D, we observed exciton miniband formation in real space and in 2D spatial confinement patterns at a specific exciton energy. Our approach provides a scalable real-space framework for exciton physics in moiré and super-moiré matter, offering a technique enabling the study of excitonic phenomena in super-moire materials.

*Acknowledgments* We acknowledge the computational resources provided by the Aalto Science-IT project and the financial support from InstituteQ, the Research Council of Finland (No. 370912), the Finnish Ministry of Education and Culture through the Quantum Doctoral Education Pilot Program (QDOC VN/3137/2024-OKM-4), the Finnish Quantum Flagship (No. 358877, Aalto University), the Finnish Centre of Excellence in Quantum Materials QMAT (No. 374166), and the ERC Consolidator Grant ULTRATWISTROICS (No. 101170477). LE acknowledges the research program “Materials for the Quantum Age” (QuMat) for financial support. This program (registration number 024.005.006) is part of the Gravitation program financed by the Dutch Ministry of Education, Culture and Science (OCW). We thank P. Liljeroth, S. Kezilebieke, P. Shen, E. Castro, B. Amorim, X. Waintal, A. Akhmerov, and C. M. Smith for useful discussions. The code used for this work can be consulted at [92].

---

\* These authors contributed equally

- [1] K. He, N. Kumar, L. Zhao, Z. Wang, K. F. Mak, H. Zhao, and J. Shan, Tightly Bound Excitons in Monolayer WSe<sub>2</sub>, *Phys. Rev. Lett.* **113**, 026803 (2014).
- [2] M. M. Ugeda, A. J. Bradley, S.-F. Shi, F. H. da Jornada, Y. Zhang, D. Y. Qiu, W. Ruan, S.-K. Mo, Z. Hussain, Z.-X. Shen, F. Wang, S. G. Louie, and M. F. Crommie, Giant bandgap renormalization and excitonic effects in a monolayer transition metal dichalcogenide semiconductor, *Nat. Mater.* **13**, 1091 (2014).
- [3] T. Mueller and E. Malic, Exciton physics and device application of two-dimensional transition metal dichalcogenide semiconductors, *npj 2D Mater. Appl.* **2**, 29 (2018).
- [4] Z. Yin, H. Li, H. Li, L. Jiang, Y. Shi, Y. Sun, G. Lu, Q. Zhang, X. Chen, and H. Zhang, Single-Layer MoS<sub>2</sub> Phototransistors, *ACS Nano* **6**, 74 (2012).
- [5] O. Lopez-Sanchez, D. Lembke, M. Kayci, A. Radenovic, and A. Kis, Ultrasensitive photodetectors based on monolayer MoS<sub>2</sub>, *Nat. Nanotech.* **8**, 497 (2013).
- [6] A. Pospischil, M. M. Furchi, and T. Mueller, Solar-energy conversion and light emission in an atomic monolayer p-n diode, *Nat. Nanotech.* **9**, 257 (2014).
- [7] J. S. Ross, P. Klement, A. M. Jones, N. J. Ghimire, J. Yan, D. G. Mandrus, T. Taniguchi, K. Watanabe, K. Kitamura, W. Yao, D. H. Cobden, and X. Xu, Electrically tunable excitonic light-emitting diodes based on monolayer WSe<sub>2</sub> p-n junctions, *Nat. Nanotech.* **9**, 268 (2014).
- [8] C.-H. Lee, G.-H. Lee, A. M. van der Zande, W. Chen, Y. Li, M. Han, X. Cui, G. Arefe, C. Nuckolls, T. F. Heinz, J. Guo, J. Hone, and P. Kim, Atomically thin p-n junctions with van der Waals heterointerfaces, *Nat. Nanotech.* **9**, 676 (2014).
- [9] M. Amani, D.-H. Lien, D. Kiriya, J. Xiao, A. Azcatl, J. Noh, S. R. Madhupathy, R. Addou, S. KC, M. Dubey, K. Cho, R. M. Wallace, S.-C. Lee, J.-H. He, J. W. Ager, X. Zhang, E. Yablonovitch, and A. Javey, Near-unity photoluminescence quantum yield in MoS<sub>2</sub>, *Science* **350**, 1065 (2015).
- [10] H. Yu, G.-B. Liu, J. Tang, X. Xu, and W. Yao, Moiré excitons: From programmable quantum emitter arrays to spin-orbit-coupled artificial lattices, *Sci. Adv.* **3**, 10.1126/sciadv.1701696 (2017).
- [11] K. L. Seyler, P. Rivera, H. Yu, N. P. Wilson, E. L. Ray, D. G. Mandrus, J. Yan, W. Yao, and X. Xu, Signatures of moiré-trapped valley excitons in MoSe<sub>2</sub>/WSe<sub>2</sub> heterobilayers, *Nature* **567**, 66 (2019).
- [12] D. A. Ruiz-Tijerina, I. Soltero, and F. Mireles, Theory of moiré localized excitons in transition metal dichalcogenide heterobilayers, *Phys. Rev. B* **102**, 195403 (2020).
- [13] E. C. Regan, D. Wang, E. Y. Paik, Y. Zeng, L. Zhang, J. Zhu, A. H. MacDonald, H. Deng, and F. Wang, Emerging exciton physics in transition metal dichalcogenide heterobilayers, *Nat. Rev. Mater.* **7**, 778 (2022).
- [14] A. de la Torre, D. M. Kennes, E. Malic, and S. Kar, Advanced Characterization of the Spatial Variation of Moiré Heterostructures and Moiré Excitons, *Small* **21**, 10.1002/sml.202401474 (2025).
- [15] L. J. M. Westenberg, L. Eek, J. D. Verbakel, K. Vonk, S. J. H. Borggreve, K. Watanabe, T. Taniguchi, P. de Boeij, R. Arouca, C. M. Smith, and P. Bampoulis, Real-Space Imaging of Moiré-Confined Excitons in Twisted Bilayer MoS<sub>2</sub>, arXiv 2511.20398 (2025).
- [16] S. Deng, H. Park, J. Reimann, J. M. Peterson, D. D. Blach, M.-J. Sun, T. Yan, D. Sun, T. Taniguchi, K. Watanabe, X. Xu, D. M. Kennes, and L. Huang, Frozen non-equilibrium dynamics of exciton mott insulators in moiré superlattices, *Nature Materials* **24**, 527–534 (2025).
- [17] Y.-M. He, G. Clark, J. R. Schaibley, Y. He, M.-C. Chen, Y.-J. Wei, X. Ding, Q. Zhang, W. Yao, X. Xu, C.-Y. Lu, and J.-W. Pan, Single quantum emitters in monolayer semiconductors, *Nat. Nanotech.* **10**, 497 (2015).
- [18] J. Frenkel, On the Transformation of light into Heat in Solids. I, *Phys. Rev.* **37**, 17 (1931).
- [19] G. H. Wannier, The Structure of Electronic Excitation Levels in Insulating Crystals, *Phys. Rev.* **52**, 191 (1937).
- [20] L. V. Keldysh, Coulomb interaction in thin semiconductor and semimetal films, *Jetp Letters* **29**, 658 (1979).
- [21] A. Chernikov, T. C. Berkelbach, H. M. Hill, A. Rigosi, Y. Li, B. Aslan, D. R. Reichman, M. S. Hybertsen, and T. F. Heinz, Exciton Binding Energy and Nonhydrogenic Rydberg Series in Monolayer WS<sub>2</sub>, *Phys. Rev. Lett.* **113**, 076802 (2014).
- [22] E. C. Marino, L. O. Nascimento, V. Sérgio Alves, N. Menezes, and C. Morais Smith, Quantum-

- electrodynamical approach to the exciton spectrum in transition-metal dichalcogenides, *2D Mater.* **5**, 041006 (2018).
- [23] M. P. Ljungberg, P. Koval, F. Ferrari, D. Foerster, and D. Sánchez-Portal, Cubic-scaling iterative solution of the Bethe-Salpeter equation for finite systems, *Phys. Rev. B* **92**, 075422 (2015).
- [24] X. Blase, I. Duchemin, D. Jacquemin, and P.-F. Loos, The Bethe-Salpeter Equation Formalism: From Physics to Chemistry, *J. Phys. Chem. Lett.* **11**, 7371 (2020).
- [25] F. Wu, T. Lovorn, and A. H. MacDonald, Theory of optical absorption by interlayer excitons in transition metal dichalcogenide heterobilayers, *Phys. Rev. B* **97**, 035306 (2018).
- [26] S. A. Herrera-González, H. A. Lara-García, G. Pirruccio, D. A. Ruiz-Tijerina, and A. Camacho-Guardian, Moiré excitons and exciton-polaritons: a review, *J. Phys.: Condens. Matter* **37**, 483002 (2025).
- [27] A. J. Uría-Álvarez, J. J. Esteve-Paredes, M. García-Blázquez, and J. J. Palacios, Efficient computation of optical excitations in two-dimensional materials with the Xatu code, *Comput. Phys. Commun.* **295**, 109001 (2024).
- [28] G. Chen, L. Jiang, S. Wu, B. Lyu, H. Li, B. L. Chittari, K. Watanabe, T. Taniguchi, Z. Shi, J. Jung, Y. Zhang, and F. Wang, Evidence of a gate-tunable Mott insulator in a trilayer graphene moiré superlattice, *Nat. Phys.* **15**, 237 (2019).
- [29] Z. Zhu, P. Cazeaux, M. Luskin, and E. Kaxiras, Modeling mechanical relaxation in incommensurate trilayer van der Waals heterostructures, *Phys. Rev. B* **101**, 224107 (2020).
- [30] A. O. Fumega, M. Niedermeier, and J. L. Lado, Correlated states in super-moiré materials with a kernel polynomial quantum tensor cross interpolation algorithm, *2D Mater.* **12**, 015018 (2025).
- [31] Y. Sun, M. Niedermeier, T. V. C. Antao, A. O. Fumega, and J. L. Lado, Self-consistent tensor network method for correlated super-moiré matter beyond one billion sites, *Physical Review Research* **7**, 10.1103/krjp-mn4v (2025).
- [32] T. V. C. Antão, Y. Sun, A. O. Fumega, and J. L. Lado, Tensor network method for real-space topology in quasicrystal Chern mosaics, [arXiv: 2506.05230](https://arxiv.org/abs/2506.05230) (2025).
- [33] A. Moustaj, Y. Sun, T. V. C. Antão, and J. L. Lado, Momentum-resolved spectral functions of super-moiré systems using tensor networks, [arXiv 2512.18397](https://arxiv.org/abs/2512.18397) (2025).
- [34] S. R. White, Density matrix formulation for quantum renormalization groups, *Phys. Rev. Lett.* **69**, 2863 (1992).
- [35] J. I. Cirac, D. Pérez-García, N. Schuch, and F. Verstraete, Matrix product states and projected entangled pair states: Concepts, symmetries, theorems, *Rev. Mod. Phys.* **93**, 045003 (2021).
- [36] M. C. Bañuls, Tensor network algorithms: A route map, *Annual Review of Condensed Matter Physics* **14**, 173–191 (2023).
- [37] R. Orús, A practical introduction to tensor networks: Matrix product states and projected entangled pair states, *Annals of Physics* **349**, 117–158 (2014).
- [38] U. Schollwöck, The density-matrix renormalization group in the age of matrix product states, *Annals of Physics* **326**, 96–192 (2011).
- [39] E. Stoudenmire and S. R. White, Studying two-dimensional systems with the density matrix renormalization group, *Annual Review of Condensed Matter Physics* **3**, 111–128 (2012).
- [40] M. Fishman, S. White, and E. Stoudenmire, The ITensor Software Library for Tensor Network Calculations, *SciPost Phys. Codebases* , 4 (2022).
- [41] M. Fishman, S. White, and E. Stoudenmire, Codebase release 0.3 for ITensor, *SciPost Phys. Codebases* , 4 (2022).
- [42] Y. Zhou, E. M. Stoudenmire, and X. Waintal, What limits the simulation of quantum computers?, *Phys. Rev. X* **10**, 041038 (2020).
- [43] W. Huggins, P. Patil, B. Mitchell, K. B. Whaley, and E. M. Stoudenmire, Towards quantum machine learning with tensor networks, *Quantum Science and Technology* **4**, 024001 (2019).
- [44] R. Orús, Tensor networks for complex quantum systems, *Nature Reviews Physics* **1**, 538–550 (2019).
- [45] G. K.-L. Chan, A. Keselman, N. Nakatani, Z. Li, and S. R. White, Matrix product operators, matrix product states, and ab initio density matrix renormalization group algorithms, *The Journal of Chemical Physics* **145** (2016).
- [46] I. Oseledets and E. Tyrtshnikov, Tt-cross approximation for multidimensional arrays, *Linear Algebra and its Applications* **432**, 70–88 (2010).
- [47] I. V. Oseledets, Tensor-train decomposition, *SIAM Journal on Scientific Computing* **33**, 2295–2317 (2011).
- [48] M. K. Ritter, Y. Núñez Fernández, M. Wallerberger, J. von Delft, H. Shinaoka, and X. Waintal, Quantics Tensor Cross Interpolation for High-Resolution Parsimonious Representations of Multivariate Functions, *Phys. Rev. Lett.* **132**, 056501 (2024).
- [49] M. Jeannin, Y. Núñez Fernández, T. Kloss, O. Parcollet, and X. Waintal, Cross-extrapolation reconstruction of low-rank functions and application to quantum many-body observables in the strong coupling regime, *Phys. Rev. B* **110**, 035124 (2024).
- [50] Y. Núñez Fernández, M. K. Ritter, M. Jeannin, J.-W. Li, T. Kloss, T. Louvet, S. Terasaki, O. Parcollet, J. von Delft, H. Shinaoka, and X. Waintal, Learning tensor networks with tensor cross interpolation: New algorithms and libraries, *SciPost Phys.* **18**, 104 (2025).
- [51] M. Ritter and contributors, [Quanticstci.jl](https://github.com/quanticstci) (2022), email: Ritter.Marc@physik.uni-muenchen.de.
- [52] M. Ritter and contributors, [Tensorcrossinterpolation.jl](https://github.com/quanticstci) (2022), email: Ritter.Marc@physik.uni-muenchen.de.
- [53] X. Waintal, C.-H. Huang, and C. W. Groth, Who can compete with quantum computers? Lecture notes on quantum inspired tensor networks computational techniques, [arXiv e-prints](https://arxiv.org/abs/2601.03035) , [arXiv:2601.03035](https://arxiv.org/abs/2601.03035) (2026), [arXiv:2601.03035 \[quant-ph\]](https://arxiv.org/abs/2601.03035).
- [54] H. Shinaoka, M. Wallerberger, Y. Murakami, K. Nogaki, R. Sakurai, P. Werner, and A. Kauch, Multiscale space-time ansatz for correlation functions of quantum systems based on quantics tensor trains, *Phys. Rev. X* **13**, 021015 (2023).
- [55] A. Erpenbeck, W.-T. Lin, T. Blommel, L. Zhang, S. Isakov, L. Bernheimer, Y. Núñez Fernández, G. Cohen, O. Parcollet, X. Waintal, and E. Gull, Tensor train continuous time solver for quantum impurity models, *Phys. Rev. B* **107**, 245135 (2023).
- [56] Y. Núñez Fernández, M. Jeannin, P. T. Dumitrescu, T. Kloss, J. Kaye, O. Parcollet, and X. Waintal, Learning feynman diagrams with tensor trains, *Phys. Rev. X* **12**, 041018 (2022).

- [57] H. Takahashi, R. Sakurai, and H. Shinaoka, Compactness of quantum tensor train representations of local imaginary-time propagators, *SciPost Phys.* **18**, 007 (2025).
- [58] M. Jeannin, Y. Núñez-Fernández, T. Kloss, O. Parcollet, and X. Waintal, Comprehensive study of out-of-equilibrium kondo effect and coulomb blockade, *Physical Review B* **112**, 10.1103/9yzc-rnzh (2025).
- [59] S. Rohshap, M. K. Ritter, H. Shinaoka, J. von Delft, M. Wallerberger, and A. Kauch, Two-particle calculations with quantum tensor trains: Solving the parquet equations, *Phys. Rev. Res.* **7**, 023087 (2025).
- [60] N. Jolly, Y. N. Fernández, and X. Waintal, Tensorized orbitals for computational chemistry, *Physical Review B* **111** (2025).
- [61] R. D. Peddinti, S. Pisoni, A. Marini, P. Lott, H. Argenti, E. Tiunov, and L. Aolita, Quantum-inspired framework for computational fluid dynamics, *Communications Physics* **7** (2024).
- [62] N. Gourianov, P. Givi, D. Jaksch, and S. B. Pope, Tensor networks enable the calculation of turbulence probability distributions, *Science Advances* **11** (2025).
- [63] M. Niedermeier, A. Moulinas, T. Louvet, J. L. Lado, and X. Waintal, Solving the gross-pitaevskii equation on multiple different scales using the quantum tensor train representation (2025), arXiv:2507.04262 [quant-ph].
- [64] A. Bou-Comas, M. Płodzień, L. Tagliacozzo, and J. J. García-Ripoll, Quantum tensor train for solving gross-pitaevskii equation (2025), arXiv:2507.03134 [cond-mat.quant-gas].
- [65] Q.-C. Chen, I.-K. Liu, J.-W. Li, and C.-M. Chung, Solving the gross-pitaevskii equation with quantum tensor trains: Ground states and nonlinear dynamics (2025), arXiv:2507.04279 [cond-mat.quant-gas].
- [66] R. J. J. Connor, C. W. Duncan, and A. J. Daley, Tensor network methods for the Gross-Pitaevskii equation on fine grids, arXiv e-prints, arXiv:2507.01149 (2025), arXiv:2507.01149 [cond-mat.quant-gas].
- [67] (2026), see Supplemental Material at [URL later] for additional details on the tensor-network construction, interleaved ordering, and the high-order delta-Chebyshev kernel, and numerical analysis.
- [68] The technical details of the implementation of the interleaved BSE Hamiltonian is discussed in the SM [67].
- [69] A. Weiße, G. Wellein, A. Alvermann, and H. Fehske, The kernel polynomial method, *Rev. Mod. Phys.* **78**, 275 (2006).
- [70] D. Jackson, On approximation by trigonometric sums and polynomials, *Transactions of the American Mathematical Society* **13**, 491–515 (1912).
- [71] J. Yi, D. Massatt, A. Horning, M. Luskin, J. H. Pixley, and J. Kaye, A high-order regularized delta-Chebyshev method for computing spectral densities, arXiv 2512.03149 (2025).
- [72] J. O. Island, A. J. Molina-Mendoza, M. Barawi, R. Biele, E. Flores, J. M. Clamagirand, J. R. Ares, C. Sánchez, H. S. J. van der Zant, R. D'Agosta, I. J. Ferrer, and A. Castellanos-Gomez, Electronics and optoelectronics of quasi-1d layered transition metal trichalcogenides, *2D Materials* **4**, 022003 (2017).
- [73] J. Ma, S. Nie, X. Gui, M. Naamneh, J. Jandke, C. Xi, J. Zhang, T. Shang, Y. Xiong, I. Kapon, N. Kumar, Y. Soh, D. Gosálbez-Martínez, O. V. Yazyev, W. Fan, H. Hübener, U. D. Giovannini, N. C. Plumb, M. Radovic, M. A. Sentef, W. Xie, Z. Wang, C. Mudry, M. Müller, and M. Shi, Multiple mobile excitons manifested as sidebands in quasi-one-dimensional metallic tase3, *Nature Materials* **21**, 423–429 (2022).
- [74] A. A. Balandin, R. K. Lake, and T. T. Salguero, One-dimensional van der Waals materials—advent of a new research field, *Applied Physics Letters* **121**, 10.1063/5.0108414 (2022).
- [75] K. Birkmeier, T. Hertel, and A. Hartschuh, Probing the ultrafast dynamics of excitons in single semiconducting carbon nanotubes, *Nature Communications* **13**, 10.1038/s41467-022-33941-2 (2022).
- [76] J. Nishida, K. Otsuka, T. Minato, Y. K. Kato, and T. Kumagai, Ultrafast infrared nano-imaging of local electron-hole dynamics in cvd-grown single-walled carbon nanotubes, *Science Advances* **11**, 10.1126/sciadv.adv9584 (2025).
- [77] Y. Tomio, H. Suzuura, and T. Ando, Interwall screening and excitons in double-wall carbon nanotubes, *Phys. Rev. B* **85**, 085411 (2012).
- [78] Y. Gong, Q. Liu, M. Gong, T. Wang, G. Zeng, W. Chan, and J. Wu, High-Performance Photodetectors Based on Effective Exciton Dissociation in Protein-Adsorbed Multiwalled Carbon Nanotube Nanohybrids, *Advanced Optical Materials* **5**, 10.1002/adom.201600478 (2017).
- [79] I. undefinedaha, A. u. Ahmad, L. Boddapatti, M. Bañobre-López, A. T. Costa, A. N. Enyashin, W. Li, P. Gargiani, M. Valvidares, J. Fernández-Rossier, and F. L. Deepak, One-dimensional cri3 encapsulated within multi-walled carbon nanotubes, *Communications Chemistry* **8**, 10.1038/s42004-025-01550-x (2025).
- [80] Q. Xu, A. Fischer, N. Tancogne-Dejean, T. Zhang, E. V. Boström, M. Claassen, D. M. Kennes, A. Rubio, and L. Xian, Engineering 2D Square Lattice Hubbard Models in 90° Twisted GeX/SnX (X = S, Se) Moiré Superlattices, *Phys Rev X* **15**, 041049 (2025).
- [81] Y.-Y. Shi, L.-M. Duan, and G. Vidal, Classical simulation of quantum many-body systems with a tree tensor network, *Phys. Rev. A* **74**, 022320 (2006).
- [82] D. C. Mattis, The few-body problem on a lattice, *Reviews of Modern Physics* **58**, 361 (1986).
- [83] A. Camacho-Guardian, L. Peña Ardila, T. Pohl, and G. Bruun, Bipolarons in a Bose-Einstein Condensate, *Phys. Rev. Lett.* **121**, 013401 (2018).
- [84] G. Mazza and A. Amarici, Strongly correlated exciton-polarons in twisted homobilayer heterostructures, *Phys. Rev. B* **106**, L241104 (2022).
- [85] T. de Sousa Araújo Cassiano, L. A. Ribeiro Júnior, G. Magela e Silva, and P. Henrique de Oliveira Neto, Strain-Tuneable Bipolaron Stability on Ultranarrow Bilayer Graphene Nanoribbon, *J. Phys. Chem. C* **128**, 1433 (2024).
- [86] T. Song, Q.-C. Sun, E. Anderson, C. Wang, J. Qian, T. Taniguchi, K. Watanabe, M. A. McGuire, R. Stöhr, D. Xiao, T. Cao, J. Wrachtrup, and X. Xu, Direct visualization of magnetic domains and moiré magnetism in twisted 2d magnets, *Science* **374**, 1140–1144 (2021).
- [87] K. C. Wong, R. Peng, E. Anderson, J. Ross, B. Yang, M. Cheng, S. Jayaram, M. Lenger, X. Zhou, Y. T. Kong, T. Taniguchi, K. Watanabe, M. A. McGuire, R. Stöhr, A. W. Tsun, E. J. G. Santos, X. Xu, and J. Wrachtrup, Super-moiré spin textures in twisted two-dimensional antiferromagnets, *Nature Nanotechnology* 10.1038/s41565-025-02103-y (2026).

- [88] Y.-H. Li and R. Cheng, Moiré magnons in twisted bilayer magnets with collinear order, *Phys. Rev. B* **102**, 094404 (2020).
- [89] S. C. Ganguli, M. Aapro, S. Kezilebieke, M. Amini, J. L. Lado, and P. Liljeroth, Visualization of Moiré Magnons in Monolayer Ferromagnet, *Nano Lett.* **23**, 3412 (2023).
- [90] Y. Li, Y. Shanguan, X. Wang, R. Liu, C. Liu, Y. Han, Z. Wang, C. Balz, R. Stewart, S.-L. Yu, J. Wen, J.-X. Li, and X. Lu, Magnetic excitations in biaxial-strain detwinned  $\alpha$ -RuCl<sub>3</sub>, [arXiv e-prints](#) , [arXiv:2509.06753](#) (2025), [arXiv:2509.06753 \[cond-mat.str-el\]](#).
- [91] D. Betto, R. Fumagalli, L. Martinelli, M. Rossi, R. Pionbo, K. Yoshimi, D. Di Castro, E. Di Gennaro, A. Sambri, D. Bonn, G. A. Sawatzky, L. Braicovich, N. B. Brookes, J. Lorenzana, and G. Ghiringhelli, Multiple-magnon excitations shape the spin spectrum of cuprate parent compounds, *Phys. Rev. B* **103**, L140409 (2021).
- [92] <https://github.com/mousanouar/Tensor-Network-Approach-to-Moire-Excitons> (2026).

# Supplemental Material: Tensor-Network methodology for super-moire excitons beyond one billion sites

Anouar Moustaj <sup>1,\*</sup> Yitao Sun <sup>1,\*</sup> Tiago V. C. Antão <sup>1</sup> Lumen Eek <sup>2</sup> and Jose L. Lado <sup>1</sup>

<sup>1</sup>*Department of Applied Physics, Aalto University, 02150 Espoo, Finland*

<sup>2</sup>*Institute of Theoretical Physics, Utrecht University, Utrecht, 3584 CC, Netherlands*

## DERIVATION OF THE EXCITON HAMILTONIAN

We consider the set of two-particle states in which a single electron is excited from the filled conduction band to the empty valence band on a lattice of  $N$  sites. Before the excitation, the many-body ground state is given by  $|\Omega\rangle = \prod_{i=1}^N c_{vl}^\dagger |0\rangle$ , in which all valence orbitals are occupied, and all conduction orbitals are empty. The set of electron-hole excitations is given by  $|l, m\rangle = c_{vl} c_{cm}^\dagger |\Omega\rangle$ , which describes a hole localized at the valence site  $l$  and an electron at the conduction site  $m$ . The basis set  $\{|l, m\rangle \mid l, m = 1, \dots, N\}$  spans the exciton quasiparticle subspace, onto which we will project the full Hamiltonian. The Hamiltonian is described by the tight-binding model of Wannier conduction and edge states, with projected local inter-band interaction, taking the form

$$\hat{H} = \sum_{b \in \{c, v\}} \sum_{lm} t_{lm}^b c_{bl}^\dagger c_{bm} + \sum_l U_l c_{vl}^\dagger c_{vl} c_{cl}^\dagger c_{cl} \equiv H_T + H_U. \quad (1)$$

To obtain the effective exciton Hamiltonian, we must calculate the matrix elements in the exciton basis,  $H_{lk, l'k'} = \langle l, k | \hat{H} | l', k' \rangle$ . First, the kinetic contribution is

$$\begin{aligned} H_{lk, l'k'}^T &= \langle l, k | \hat{H}_T | l', k' \rangle \\ &= \sum_{b \in \{c, v\}} \sum_{ij} t_{ij}^b \langle \Omega | c_{ck} c_{vl}^\dagger c_{bi}^\dagger c_{bj} c_{v'l'} c_{ck'}^\dagger | \Omega \rangle \\ &= \sum_{b \in \{c, v\}} \sum_{ij} t_{ij}^b \langle \Omega | c_{vl}^\dagger (\delta_{bc} \delta_{ki} - c_{bi}^\dagger c_{ck}) (\delta_{bc} \delta_{k'j} - c_{ck'}^\dagger c_{bj}) c_{v'l'} | \Omega \rangle \\ &= \sum_{b \in \{c, v\}} \sum_{ij} t_{ij}^b \delta_{bc} \delta_{ki} \delta_{k'j} \langle \Omega | c_{vl}^\dagger c_{v'l'} | \Omega \rangle + \sum_{b \in \{c, v\}} \sum_{ij} t_{ij}^b \langle \Omega | c_{vl}^\dagger c_{bi}^\dagger c_{ck} c_{ck'}^\dagger c_{bj} c_{v'l'} | \Omega \rangle. \end{aligned}$$

In the last term, the cross-terms in the expansion vanish. This can be seen by commuting the conduction creation/annihilation operator and acting it on the Fermi sea. Upon further simplification,

$$\begin{aligned} H_{lk, l'k'}^T &= \sum_{b \in \{c, v\}} \sum_{ij} t_{ij}^b \delta_{bc} \delta_{ki} \delta_{k'j} \langle \Omega | (\delta_{ll'} - c_{v'l'} c_{vl}^\dagger) | \Omega \rangle + \sum_{b \in \{c, v\}} \sum_{ij} t_{ij}^b \langle \Omega | c_{vl}^\dagger c_{bi}^\dagger (\delta_{kk'} - c_{ck'}^\dagger c_{ck}) c_{bj} c_{v'l'} | \Omega \rangle \\ &= t_{kk'}^c \delta_{ll'} + \sum_{b \in \{c, v\}} \sum_{ij} t_{ij}^b \delta_{kk'} \langle \Omega | c_{bi}^\dagger c_{vl}^\dagger c_{v'l'} c_{bj} | \Omega \rangle \\ &= t_{kk'}^c \delta_{ll'} + \sum_i t_{ii}^v \delta_{kk'} \delta_{ll'} - \sum_{b \in \{c, v\}} \sum_{ij} t_{ij}^b \delta_{kk'} \langle \Omega | c_{bi}^\dagger c_{v'l'} c_{vl}^\dagger c_{bj} | \Omega \rangle \\ &= t_{kk'}^c \delta_{ll'} + \sum_i t_{ii}^v \delta_{kk'} \delta_{ll'} - \sum_{b \in \{c, v\}} \sum_{ij} t_{ij}^b \delta_{kk'} \delta_{bv} \delta_{l'i} \delta_{lj} \\ &= t_{kk'}^c \delta_{ll'} - t_{l'l}^v \delta_{kk'} + \sum_i t_{ii}^v \delta_{kk'} \delta_{ll'}. \end{aligned}$$

Here, the first term describes the hopping of the excited conduction electron. The second term corresponds to the hopping of the valence hole. The last term is a constant energy shift originating from the filled Fermi sea. It is diagonal in the exciton indices, such that it shifts all exciton energies and can be absorbed into a redefinition of the total energy.

Now, for the interaction term, we have

$$\begin{aligned}
H_{lk,l'k'}^U &= \langle l, k | \hat{H}_U | l', k' \rangle \\
&= \sum_i U_i \langle \Omega | c_{ck} c_{vl}^\dagger c_{vi}^\dagger c_{vi} c_{ci}^\dagger c_{ci} c_{vl'} c_{ck'}^\dagger | \Omega \rangle \\
&= - \sum_i U_i \delta_{ik'} \langle \Omega | c_{ck} c_{vl}^\dagger c_{vi}^\dagger c_{vi} c_{ci}^\dagger c_{vl'} | \Omega \rangle \\
&= - \sum_i U_i \delta_{ik'} \langle \Omega | c_{ck} c_{vl}^\dagger c_{ci}^\dagger c_{vl'} | \Omega \rangle + \sum_i U_i \delta_{ik'} \langle \Omega | c_{ck} c_{vl}^\dagger c_{vi}^\dagger c_{vi} c_{ci}^\dagger c_{vl'} | \Omega \rangle \\
&= \sum_i U_i \delta_{ik'} \delta_{ik} \delta_{ll'} - \sum_i U_i \delta_{ik'} \delta_{il} \delta_{ik} \delta_{il'} \\
&= U_k \delta_{kk'} \delta_{ll'} - U_k \delta_{kk'} \delta_{ll'} \delta_{kl}.
\end{aligned}$$

The second term is the driving mechanism of bound exciton formation and is nonzero when  $k = l$ , i.e., when electron and hole occupy the same site, capturing the local electron-hole Coulomb interaction.

To identify the physically relevant excitation energies, we subtract the ground-state energy  $E_\Omega = \langle \Omega | \hat{H} | \Omega \rangle$ . First, we treat the kinetic term

$$\begin{aligned}
\langle \Omega | \hat{H}_T | \Omega \rangle &= \sum_{b \in \{c, v\}} \sum_{ij} t_{ij}^b \langle \Omega | c_{bi}^\dagger c_{bj} | \Omega \rangle \\
&= \sum_{ij} t_{ij}^v \langle \Omega | c_{vi}^\dagger c_{vj} | \Omega \rangle \\
&= \sum_i t_{ii}^v.
\end{aligned}$$

The interaction term, on the other hand is trivially  $\langle \Omega | \hat{H}_U | \Omega \rangle = 0$ . Thus  $E_\Omega = \sum_i t_{ii}^v$ . Since the filled valence sea contributes a constant background energy, we can subtract it from the effective exciton Hamiltonian to obtain

$$\begin{aligned}
H_{lk,l'k'} &= \langle l, k | \hat{H} | l', k' \rangle - E_\Omega \delta_{kk'} \delta_{ll'} \\
&= (t_{kk'}^c + U_k \delta_{kk'}) \delta_{ll'} - t_{l'l}^v \delta_{kk'} - U_k \delta_{kk'} \delta_{ll'} \delta_{kl}.
\end{aligned}$$

Written in operator form, this yields

$$\hat{H}_X = \hat{T}_c \otimes \mathbb{1} - \mathbb{1} \otimes \hat{T}_v - \hat{U}_X \quad (2)$$

where  $\hat{T}_c$  contains both the conduction hopping term and an additional contribution from the interaction. The last term couples electrons and holes and cannot be written as a product operator.

## CONSTRUCTION OF THE INTERLEAVED-ORDER MPO FOR GENERAL EXCITONIC HAMILTONIANS

We present the details of the construction of the Matrix Product Operator (MPO) employing an interleaved ordering strategy for general excitonic systems. While the Bethe-Salpeter Equation (BSE) serves as our primary illustrative example, this framework is inherently applicable to any  $d$ -dimensional tight-binding Hamiltonian where degrees of freedom can be partitioned into distinct sub-lattices or directions.

First, we construct independent Hamiltonian MPOs for the electron ( $e$ ) and hole ( $h$ ) sectors,  $\hat{\mathcal{H}}_e$  and  $\hat{\mathcal{H}}_h$  respectively, using the standard site ordering as in Refs. [1–3]. For a system defined by  $2^L$  spatial sites, these operators act separately on the local electron pseudo-spin basis  $(s_{e_1}, s_{e_2}, \dots, s_{e_L})$  and hole pseudo-spin basis  $(s_{h_1}, s_{h_2}, \dots, s_{h_L})$  respectively. Subsequently, these individual MPOs are expanded into a unified  $2L$ -site Hilbert space through the insertion of  $\delta$ -tensors between adjacent blocks, as shown in Fig. 1(a). There, we see that we implement a mapping where the electron degrees of freedom occupy the odd-numbered sites, and the hole degrees of freedom occupy the even-numbered sites. The  $\delta$ -tensors function as identity mappings that preserve the integrity of the electron and hole blocks, preventing unphysical coupling during the expansion. By summing these expanded operators, we obtain the complete interleaved MPO, resulting in a basis of the form  $(s_{e_1}, s_{h_1}, s_{e_2}, s_{h_2}, \dots, s_{e_L}, s_{h_L})$ , and effectively placing corresponding electron

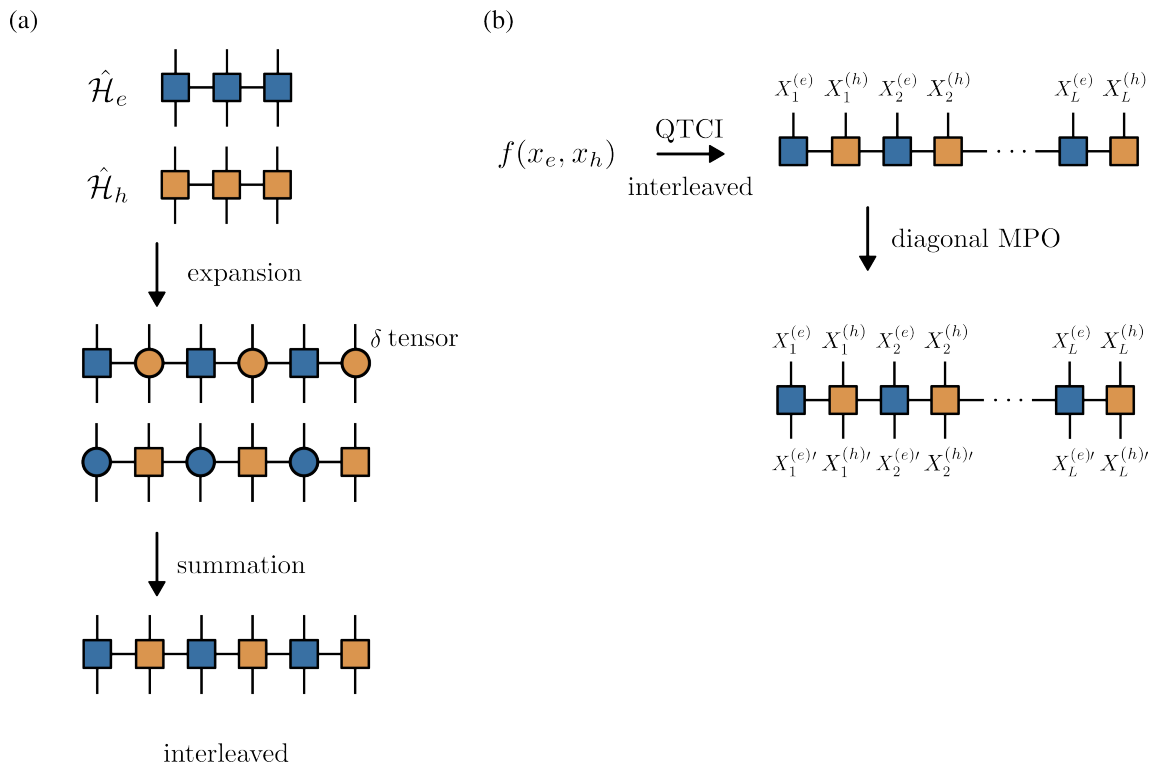


FIG. 1. (a) The construction of the interleaved ordering for the Hamiltonian MPO. (b) An arbitrary function  $f(x_e, x_h)$  of the electron and hole position is efficiently represented in interleaved order using QTCI and its promotion to a diagonal MPO.

and hole sites in immediate physical proximity along the chain. The resulting MPO is then simply  $\hat{\mathcal{H}}_e \otimes \hat{\mathcal{H}}_h$  expressed in the interleaved order.

For the treatment of the correlated term  $\hat{U}$  in Eq. (2), any spatial dependence of the form  $U(\mathbf{r}_e, \mathbf{r}_h)$  can be directly implemented by learning the tensor network representation with Quantics Tensor Train Cross Interpolation (QTCI) [4, 5]. Since the QTCI algorithm naturally performs multi-dimensional interpolation using a bit-interleaved order, it will generate matrix product states (MPS) that are intrinsically compatible with our interleaved basis. This eliminates the need for manual index remapping and ensures that interaction terms are treated optimally in the interleaved representation, as shown in Fig. 1(b).

The primary physical motivation for adopting this interleaved ordering lies in the preservation of operator locality and the subsequent reduction of the MPO bond dimension  $\chi$ . As derived in the previous section, Eq. (2) shows that for the highly localized excitonic system we are considering, the interaction term  $U(\mathbf{r}_e, \mathbf{r}_h)$  only exists for electrons and holes at the same physical sites:

$$U(\mathbf{r}_e, \mathbf{r}_h) = \begin{cases} U_0, & \mathbf{r}_e = \mathbf{r}_h \\ 0, & \mathbf{r}_e \neq \mathbf{r}_h \end{cases}. \quad (3)$$

In a minimal basis where all electrons precede all holes as  $(s_{e_1}, s_{e_2}, \dots, s_{e_L}, s_{h_1}, s_{h_2}, \dots, s_{h_L})$ , the MPO representation of Eq. (3) is  $\hat{U} = U_0 \prod_{r=1}^L (\frac{1}{2} \mathbb{1}_r \otimes \mathbb{1}_{r+L} + 2\sigma_r^z \sigma_{r+L}^z)$ . This operator necessitates capturing correlations between sites separated by a distance of  $L$ . Consequently, the MPO bond dimension  $\chi$  scales as  $2^L$  to account for these long-range entanglements. Conversely, in the interleaved basis  $(s_{e_1}, s_{h_1}, s_{e_2}, s_{h_2}, \dots, s_{e_L}, s_{h_L})$ , the same interaction becomes strictly local, involving only adjacent sites. This locality allows the operator to be represented by a small and constant bond dimension that is independent of  $L$ , namely  $\chi = 2$  in our case. By distributing physical correlations more uniformly and locally across the tensor network, this ordering effectively mitigates the exponential growth of the bond dimension, thereby significantly enhancing both numerical precision and computational stability during large-scale simulations.

Finally, it should be emphasized that the interleaved MPO is mathematically equivalent to the minimal basis discussed above, differing only by a permutation of the matrix elements. This representation preserves the Hamiltonian's spectrum while providing a vastly more efficient framework for tensor network calculations.

## DETAILS OF THE HIGH-ORDER DELTA-Chebyshev KERNEL

Here, we briefly discuss the high-order delta-Chebyshev (HODC) kernel [6] used in the calculation of two-dimensional systems in the main text. The motivation of the HODC kernel is to use an  $m^{\text{th}}$  order rational approximation of  $\delta(\omega - E)$  by using

$$K_\eta(\omega, E) = -\frac{1}{\pi} \sum_{l=1}^m \text{Im} \frac{w_l}{\omega - E + \eta z_l}. \quad (4)$$

Here, the weights  $w_l$  and poles  $z_l$  are both complex numbers and need to satisfy specific matching conditions for this approximation to hold. This is enforced by solving the Vandermonde system of linear equations [7]

$$\begin{bmatrix} 1 & 1 & \dots & 1 \\ z_1 & z_2 & \dots & z_m \\ \vdots & \vdots & \ddots & \vdots \\ z_1^{m-1} & z_2^{m-1} & \dots & z_m^{m-1} \end{bmatrix} \begin{bmatrix} w_1 \\ w_2 \\ \vdots \\ w_m \end{bmatrix} = \begin{bmatrix} 1 \\ 0 \\ \vdots \\ 0 \end{bmatrix}. \quad (5)$$

The solutions  $w_l$  result in a kernel  $K_\eta(\omega, E)$  that approximates  $\delta(\omega - E)$  with an accuracy of order  $\mathcal{O}(\eta^m)$  (see Ref. [6] for a proof). In practice, for  $m < 8$ , the solutions  $w_l$  can be calculated to double precision. Then, to approximate the kernel  $K_\eta(\omega, E)$ , we can use a Chebyshev expansion

$$K_\eta(\omega, E) \approx \sum_{k=0}^{N_\nu-1} \nu_k(\omega, \eta) T_k(E), \quad (6)$$

where the number of moments  $N_\nu$  should be of order  $\mathcal{O}(1/\eta)$  to achieve a precise approximation [6]. With this, we can calculate the local density of state (LDOS) at site  $i$  of a Hamiltonian  $H$  as

$$D_i(\omega) = \langle i | \delta(\omega - H) | i \rangle \approx \sum_{k=0}^{N_\nu-1} \nu_k(\omega, \eta) \langle i | T_k(H) | i \rangle, \quad (7)$$

where  $T_k(H)$  is the  $k$ -th order Chebyshev polynomial of  $H$ . Finally, to acquire the expansion coefficients  $\nu_k(\omega, \eta)$  for given  $\omega$  and  $\eta$ , we first solve Eq. 5 to obtain the weights  $w_l$ . Subsequently, we sample  $n$  values of  $E$  at the Chebyshev nodes (roots of the  $n$ -th Chebyshev polynomial),

$$E_j = \cos\left(\frac{(j + \frac{1}{2})\pi}{n}\right), \quad j = 0, 1, \dots, n-1. \quad (8)$$

The coefficients  $\nu_k$  are then obtained by projecting the function onto the Chebyshev basis. This projection is mathematically equivalent to a Discrete Cosine Transform (DCT):

$$\nu_k(\omega, \eta) = \frac{2 - \delta_{k0}}{n} \sum_{j=0}^{n-1} K_\eta(\omega, E_j) \cos\left(\frac{k(j + \frac{1}{2})\pi}{n}\right), \quad (9)$$

This allows for the rapid acquisition of all  $p$  terms of  $\nu_k(\omega, \eta)$ , which are subsequently used to evaluate the exciton LDOS via Eq. 7. By applying the HODC kernel to the calculation of the kernel polynomial algorithm, the convergence performance can reach accuracy of order  $\mathcal{O}(\eta^m) \approx \mathcal{O}(1/N_\nu^m)$ , which is superior compared to the convergence performance of the Jackson kernel,  $\mathcal{O}(1/N_\nu^2)$ .

Despite its superior convergence properties, the primary drawback of the HODC kernel is the lack of guaranteed positivity, in contrast to traditional truncation kernels (e.g., Jackson or Lorentz kernels) [8, 9]. This characteristic may introduce minor numerical artifacts in the calculation of the excitonic LDOS, which is physically required to be non-negative. However, these errors are typically sufficiently small to be neglected when weighed against the kernel's rapid convergence. More importantly, within our tensor-network-based KPM framework, the application of the HODC kernel enables the attainment of high-precision LDOS with significantly fewer Chebyshev recursion iterations. This reduction in the expansion order  $N_\nu$  is crucial, as it drastically decreases the amount bond dimension truncations required during MPO-MPS contractions and MPS-MPS summations. In the context of high-order recursions, the

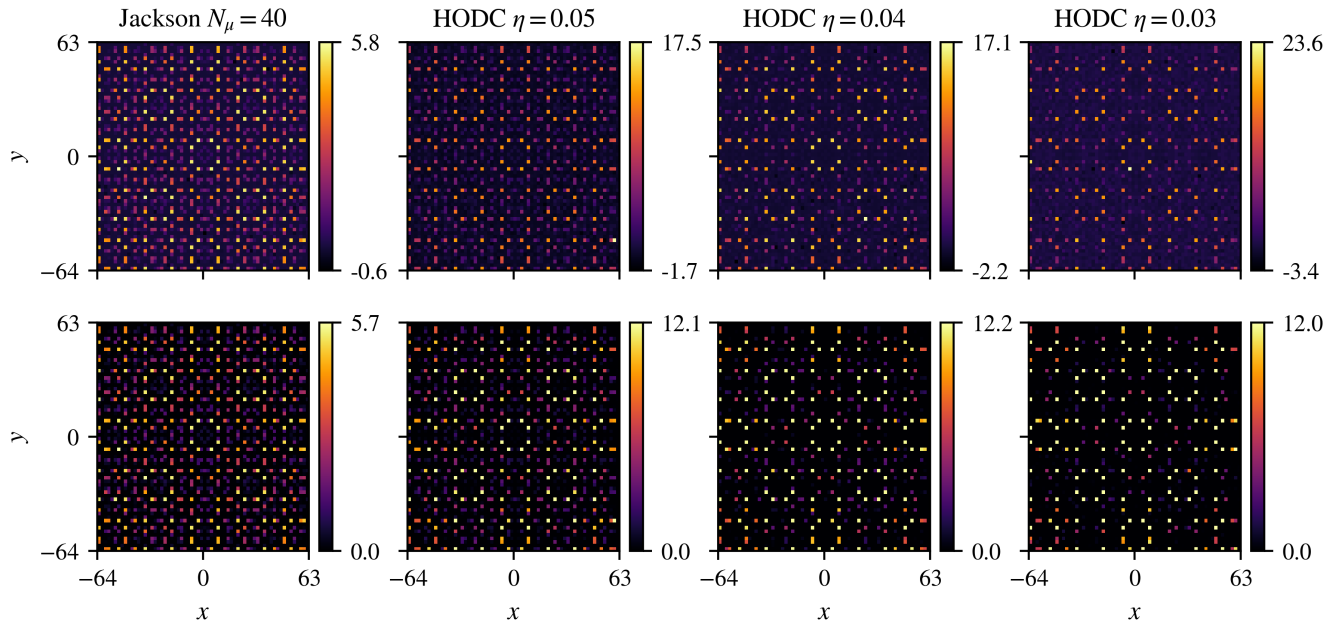


FIG. 2. Comparison of the performance of the Jackson and HODC kernels at  $N_\mu = 40$  for the two-dimensional system considered in the main text, focusing on atomic-scale resolution. The top row displays the raw results, where negative artifacts arise from tensor-network compression and, in the case of HODC, from the kernel's intrinsic properties. The bottom row shows a cleaned version of the data, in which selected peak values have been reduced, and all minimal values have been set to zero. In all cases,  $N_\mu = 40$  and  $m = 3$ .

cumulative truncation error inherent in tensor network operations often poses a more significant challenge to precision than the non-positivity of the kernel. Therefore, the HODC kernel not only enhances computational efficiency but also preserves overall accuracy by mitigating the accumulation of truncation noise, rendering its minor non-positive deviations a justifiable and negligible trade-off.

To illustrate this, we compare the performance of the Jackson and HODC kernels in resolving the exciton LDOS at the modest number of moments  $N_\mu = 40$ , which represents the current limit accessible within our tensor-network framework. In these calculations, we use  $m = 3$ , which already provides improved resolution compared to the Jackson kernel, as shown in Fig. 2. A higher value of  $m$  while keeping  $N_\mu = 40$  will increase the negativity, as can be seen from Eq. (5), where  $m$  enters as a power of the complex poles  $z_l$  of Eq. (4), therefore increasing the amplitude and frequency of oscillations. For this reason, we do not consider it in this work. As  $\eta$  decreases towards its ideal value of  $1/N_\mu$ , spectral broadening is reduced, and finer spatial features become more clearly resolved. This increased resolution, however, is accompanied by enhanced negative values in the density, arising both from tensor-network compression and from the intrinsic oscillatory nature of the HODC kernel. In the bottom row of Fig. 2, we present a cleaned version of the raw data, in which negative values of  $\rho$  are manually set to zero and selected spurious high-intensity pixels are suppressed to improve visual clarity.

\* These authors contributed equally

- [1] Y. Sun, M. Niedermeier, T. V. C. Antão, A. O. Fumega, and J. L. Lado, Self-consistent tensor network method for correlated super-moiré matter beyond one billion sites, *Phys. Rev. Res.* **7**, 043288 (2025).
- [2] T. V. C. Antão, Y. Sun, A. O. Fumega, and J. L. Lado, Tensor network method for real-space topology in quasicrystal Chern mosaics, arXiv: 2506.05230 (2025).
- [3] A. Moustaj, Y. Sun, T. V. C. Antão, and J. L. Lado, Momentum-resolved spectral functions of super-moiré systems using tensor networks, arXiv 2512.18397 (2025).
- [4] M. K. Ritter, Y. Núñez Fernández, M. Wallerberger, J. von Delft, H. Shinaoka, and X. Waintal, Quantics Tensor Cross Interpolation for High-Resolution Parsimonious Representations of Multivariate Functions, *Phys. Rev. Lett.* **132**, 056501 (2024).
- [5] Y. Núñez Fernández, M. K. Ritter, M. Jeannin, J.-W. Li, T. Kloss, T. Louvet, S. Terasaki, O. Parcollet, J. von Delft,

- H. Shinaoka, and X. Waintal, Learning tensor networks with tensor cross interpolation: New algorithms and libraries, *SciPost Phys.* **18**, 104 (2025).
- [6] J. Yi, D. Massatt, A. Horning, M. Luskin, J. H. Pixley, and J. Kaye, A high-order regularized delta-Chebyshev method for computing spectral densities, arXiv 2512.03149 (2025).
- [7] M. Colbrook, A. Horning, and A. Townsend, Computing Spectral Measures of Self-Adjoint Operators, *SIAM Review* **63**, 489 (2021).
- [8] A. Weiße, G. Wellein, A. Alvermann, and H. Fehske, The kernel polynomial method, *Rev. Mod. Phys.* **78**, 275 (2006).
- [9] D. Jackson, On approximation by trigonometric sums and polynomials, *Transactions of the American Mathematical Society* **13**, 491–515 (1912).